



## Microstructural defects in hot deformed and as-transformed $\tau$ -MnAl-C

P. Zhao <sup>a, b, \*</sup>, L. Feng <sup>a, b</sup>, K. Nielsch <sup>a, b</sup>, T.G. Woodcock <sup>a</sup>

<sup>a</sup> Leibniz IFW Dresden, Institute for Metallic Materials, Helmholtzstr. 20, 01069, Dresden, Germany

<sup>b</sup> TU Dresden, Institute of Materials Science, 01062, Dresden, Germany



### ARTICLE INFO

#### Article history:

Received 13 July 2020

Received in revised form

20 August 2020

Accepted 1 September 2020

Available online 2 September 2020

#### Keywords:

MnAl magnet

Hot deformation

Defects

Transmission electron microscopy (TEM)

### ABSTRACT

In this study, detailed microstructural characterisation has been conducted in both as-transformed and hot deformed samples of  $\tau$ -MnAl-C using transmission electron microscopy. After hot deformation, true twins, dislocations, intrinsic stacking faults and precipitates of  $Mn_3AlC$  are the main defects in the recrystallised grains. True twins and order twins were distinguished based on differences in their diffraction patterns. A significant fraction of non-recrystallised grains existed, which had microstructures based on combinations of high densities of true twins, dislocations, and deformation bands. The formation of the  $Mn_3AlC$  precipitates was confirmed and related to the reduction of saturation magnetization and the increase in the Curie temperature of  $\tau$ -MnAl-C after hot deformation. Antiphase boundaries, which are believed to act as nucleation sites for reverse domains, were not observed in the hot deformed sample.

© 2020 The Authors. Published by Elsevier B.V. This is an open access article under the CC BY license (<http://creativecommons.org/licenses/by/4.0/>).

### 1. Introduction

The ferromagnetic phase  $\tau$ -MnAl-C is a highly promising rare earth free permanent magnet both in terms of its magnetic properties and the non-critical nature of the raw elements [1–5]. Its potential role to replace certain types of Nd-Fe-B magnets would partially relieve the pressure on rare earth resources [6,7]. The best magnetic properties to date have been achieved in hot extruded  $\tau$ -MnAl-C reported by Ohtani et al. [8] with a maximum energy product of  $(BH)_{\max} = 56 \text{ kJm}^{-3}$ , coercivity of  $iH_c = 0.3 \text{ T}$  and remanence of  $J_r = 0.61 \text{ T}$ . As the highest possible maximum energy product for this material is estimated at  $(BH)_{\max} = 110 \text{ kJm}^{-3}$  [3,9], large further improvements in measured magnetic properties should be possible.

The ferromagnetic  $\tau$  phase ( $P4/mmm$ , AuCu I type), which is metastable [10,11], can be formed from the high temperature  $\epsilon$  phase ( $P6_3/mmc$ , Mg type). Two mechanisms have been proposed to describe this transformation and they are massive transformation [12–14] and the displacive-diffusional mechanism [15–17]. Both mechanisms could occur simultaneously during the phase transformation from  $\epsilon$  to  $\tau$ , but the massive transformation is thought to be dominant in polycrystals and at temperatures above  $500 \text{ }^\circ\text{C}$  [18]. After the  $\tau$ -phase has been formed, the material is referred to as being in the as-transformed state. A hot deformation

process is then applied to the as-transformed material in order to improve the magnetic properties. In both as-transformed and hot deformed states, the microstructure of the material is characterized by the presence of many different types of defects, like dislocations, twins, stacking faults, antiphase boundaries and grain boundaries. All of these have a crucial influence on the magnetic properties due to their interactions with magnetic domain walls [3,19–22]. Detailed characterisation of these defects can be used as input for micromagnetic simulations [23][24], which will provide new insight about the magnetic interactions of these defects. With this knowledge, further improvements in the magnetic properties may be achieved through tailoring the processing route in order to exclude those defects which are deleterious.

Previous research has shown that the defect population and microstructure change radically after hot deformation [19,21,22,25,26]. Due to the interest in the transformation mechanism of  $\tau$ -MnAl from the high temperature  $\epsilon$  phase, detailed results of various defects in as-transformed  $\tau$ -MnAl have been presented by many researchers using transmission electron microscopy (TEM) [12–16,18,27,28] and it is confirmed that many defects are produced during the phase transformation. Yanar et al. [12] reported the formation of high density of defects is attributed to the growth faults during atomic attachment at the migrating interface of  $\epsilon$  and  $\tau$  phases. In spite of the superior magnetic properties of the hot deformed state, detailed studies of defects in hot deformed  $\tau$ -MnAl-C using TEM are rare [21,22,26] and none of them have carried out detailed characterisation of the defects in the non-recrystallised grains. It has been reported that the existence of

\* Corresponding author. Leibniz IFW Dresden, Institute for Metallic Materials, Helmholtzstr. 20, 01069, Dresden, Germany.

E-mail address: [p.zhao@ifw-dresden.de](mailto:p.zhao@ifw-dresden.de) (P. Zhao).

non-recrystallised grains in the hot deformed  $\tau$ -MnAl is detrimental to coercivity [19], therefore detailed TEM study about non-recrystallised grains is highly desirable.

In this study,  $\tau$ -MnAl-C was hot deformed through the die upsetting process. This process is analogous to hot extrusion in that dynamic recrystallization and texture formation also occur. Die-upset MnAl-C magnets have a radial texture and therefore, ring magnets for motor applications could be prepared through this method [29]. Detailed TEM studies of the as-transformed and hot deformed states were then carried out.

## 2. Experimental

An alloy with the nominal composition of  $\text{Mn}_{53}\text{Al}_{45}\text{C}_2$  (at.%) was prepared from high purity elemental starting materials (99.99% Mn, 99.99% Al and 99.9% C) by induction melting under argon atmosphere and casting into a cylindrical Cu mould with 10 mm diameter. The as-cast samples were encapsulated in a quartz tube filled with pure Ar at a back pressure of 150 mbar, homogenized at 1100 °C for 2 days, followed by air cooling to room temperature to obtain the  $\tau$ -phase. This sample will be referred to as 'as-transformed sample'. Samples with size 10 mm in diameter and 8 mm in length were cut from the as-transformed sample and then subjected to die upsetting at 700 °C with a logarithmic degree of deformation of 1.386 and constant strain rate of 0.001 s<sup>-1</sup>. This sample will be referred to as 'hot deformed sample'. Before the start of die upsetting, the temperature was held for 10 min to homogenize the temperature within the sample.

The magnetic properties were measured using a Quantum Design PPMS with applied fields up to 14 T at room temperature. Thermomagnetic measurements were conducted by the PPMS with an applied field of 0.1 T. The Curie temperature was defined as the minimum of the first derivative of this data. The magnetization data were corrected for the effect of self-demagnetization and the demagnetization factors were calculated based on the method proposed by Aharoni [30].

The lattice parameters of the  $\tau$  phase in the as-transformed and hot deformed states were obtained using Rietveld refinement method of x-ray diffraction (XRD) patterns obtained with Co-K $\alpha$  radiation using a Bruker diffractometer. The refined lattice parameters were obtained by analysing the complete 2 $\theta$  range of 20°–120°.

Samples were prepared for scanning electron microscopy using standard metallographic grinding and polishing techniques. The microstructure of the samples was imaged in backscattered electron (BSE) mode in a Zeiss Leo 1530 scanning electron microscope (SEM) equipped with a field emission gun. For TEM analysis, the foils sliced from the two materials were prepared by mechanical grinding to a thickness of 20–50  $\mu\text{m}$ , followed by Ar-ion milling at 4.5 kV under a low beam angle of 11–13°. The foil taken from the hot deformed sample was oriented so that the direction normal to the foil was perpendicular to the compression axis. TEM studies were performed using a FEI Tecnai G<sup>2</sup> microscope operated at 200 kV with energy-dispersive X-ray spectroscopy (EDXS). For all the diffraction analysis, the *tp4* representation of the L1<sub>0</sub> unit cell ( $a = b = 3.92 \text{ \AA}$ ,  $c = 3.57 \text{ \AA}$ ,  $\alpha = \beta = \gamma = 90^\circ$ ) will be used. The Burgers vector of dislocations was identified using the conventional invisibility criterion  $\mathbf{g} \cdot \mathbf{b} = 0$ , where  $\mathbf{g}$  is the diffraction vector and  $\mathbf{b}$  is the Burgers vector. The magnitude of the Burgers vector was determined from the number of thickness fringes ( $n$ ) terminating at the exit of the dislocation in weak-beam dark field (WBDF) images, which is related to the relation  $\mathbf{g} \cdot \mathbf{b} = n$  [31,32]. The intrinsic or extrinsic nature of stacking faults was determined based on the outermost fringes in the bright field (BF) and dark field (DF) images, which is associated with the phase shift  $\alpha = 2\pi\mathbf{g} \cdot \mathbf{R}_F$ , where  $\mathbf{g}$  is the diffraction vector and  $\mathbf{R}_F$  is the displacement vector of the fault [33].

## 3. Results and discussion

### 3.1. Magnetic properties and microstructure in the as-transformed and hot deformed states

The magnetic hysteresis loops of the  $\tau$ -MnAl-C samples before and after hot deformation are shown in Fig. 1(a). The as-transformed sample shows a low coercivity ( $\mu_0 H_c = 0.017 \text{ T}$ ) and remanence ( $J_r = 0.17 \text{ T}$ ), and its magnetic properties are isotropic *i.e.* hysteresis loops measured parallel to different sample axis are identical. After hot deformation, the remanence and coercivity are much higher than in the as-transformed state and the properties are anisotropic (cf. radial and axial curves in Fig. 1(a)). The increase of remanence in hot deformed sample implies  $\langle 00l \rangle$  texture formation and this could be confirmed from the XRD results as the (002) intensity decreases by 19% and (200) peak intensity increases by 9% after hot deformation (Supplementary Fig. S1). These results suggest more crystals are aligned with  $\langle 00l \rangle$  direction perpendicular to the axial direction compared to as-transformed sample. The remanence measured in the radial direction ( $J_r = 0.39 \text{ T}$ ) is higher than the value measured in the axial direction ( $J_r = 0.30 \text{ T}$ ), which indicates that the magnetically easy  $\langle 001 \rangle$  axis of the grains has a preferred orientation in the plane perpendicular to the axial direction. The degree to which this alignment occurs can be quantified using the relation:

$$\omega = (J_r^{\parallel} - J_r^{\perp}) / J_r^{\parallel} \quad (1)$$

where  $J_r^{\parallel}$  and  $J_r^{\perp}$  are the remanence measured parallel and perpendicular to the texture axis. A degree of texture,  $\omega = 0.23$  was found for the hot deformed sample. The maximum degree of texture which can be achieved by die-upsetting is necessarily lower than that achievable via extrusion because in die-upset samples as the preferred alignment occurs in the plane perpendicular to the axis of the applied force rather than in the direction parallel to it, as is the case for extrusion. The coercivity of the hot deformed sample measured in the radial and axial direction is similar ( $\mu_0 H_c = 0.16 \text{ T}$ ).

According to the result of fitting the approach to saturation for the as-transformed sample, the saturation polarisation is around  $J_{\text{sat}} = 0.82 \text{ T}$  (inset in Fig. 1(a)). A slightly lower saturation polarisation (40 mT lower) is observed for the hot deformed  $\tau$ -MnAl-C alloy measured in both directions. The Curie temperature (Fig. 1(b)) increases by 30 K after hot deformation compared to the value of 513 K for the as-transformed  $\tau$ -MnAl-C alloy.

The microstructures of the as-transformed and hot deformed samples are shown by the backscattered electron (BSE) images in Fig. 2. The dramatic grain refinement due to the dynamic recrystallization during hot deformation can be clearly seen (note that the scalebars are different for the two images). The other main visible differences (white arrows in Fig. 2(b)) to the as-transformed state are i) the presence of precipitates of other phases and ii) the presence of polytwinned, non-recrystallised grains.

In order to explain the reasons for the observed changes in magnetic properties and to further investigate the microstructural differences, detailed characterisation of the defects in both states was conducted by transmission electron microscopy (TEM).

### 3.2. Defect structures in as-transformed $\tau$ -MnAl-C

#### 3.2.1. Dislocations

An inhomogeneous distribution of dislocations was observed in the as-transformed  $\tau$ -MnAl-C sample and grain with medium dislocation density was chosen for investigation here. To determine the Burgers vectors of the various dislocations observed,

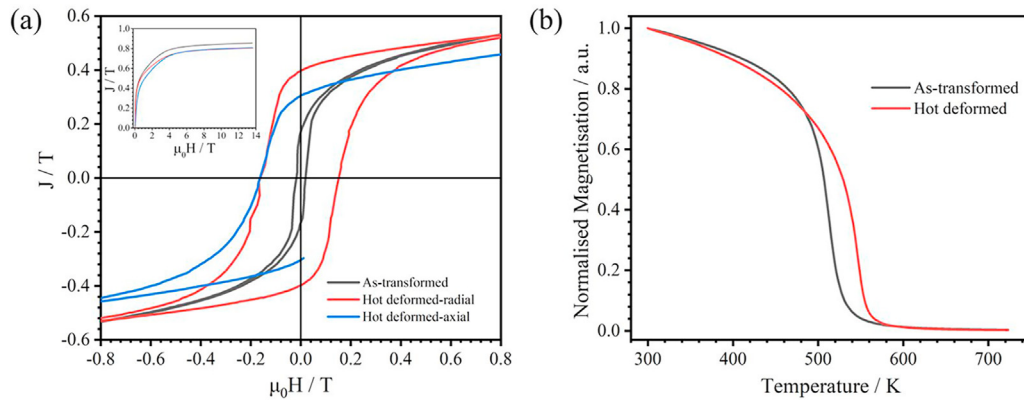


**Fig. 1.** (a) Hysteresis loops of hot deformed  $\tau$ -MnAl-C sample measured in radial (red line) and axial (blue line) directions, and as-transformed  $\tau$ -MnAl-C sample (black line). The inset shows the hysteresis loop of samples under maximum applied field of 14 T in the first quadrant. The curves were corrected for demagnetizing effects. (b) Curie temperature of as-transformed and hot deformed  $\tau$ -MnAl-C. (For interpretation of the references to colour in this figure legend, the reader is referred to the Web version of this article.)

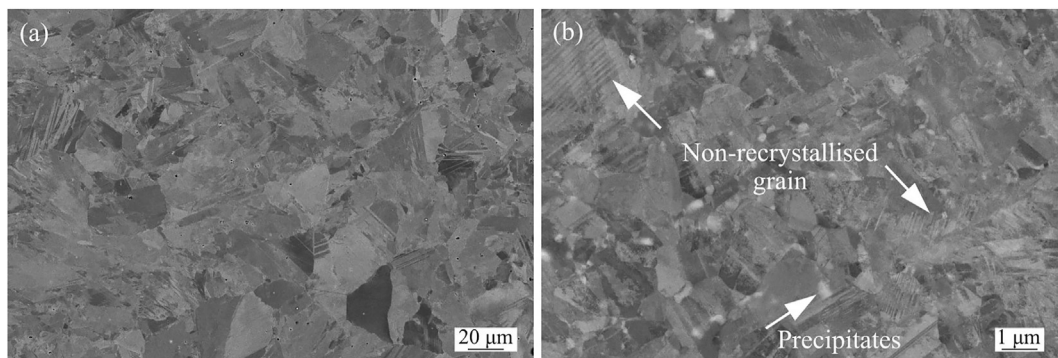


**Fig. 2.** Backscattered electron (BSE) images of as-transformed (a) and hot deformed (b)  $\tau$ -MnAl-C samples.

contrast analysis using different diffraction conditions was carried out (Fig. 3). Selected area electron diffraction (SAED) patterns (insets in Fig. 3(a) and (f)) confirm that the grain corresponds to  $\tau$ -MnAl-C with the beam parallel to the [001] and [103] zone axis, respectively. Fig. 3(b)–(e) present bright field images (BF) of dislocations under two-beam conditions using diffraction vectors  $\mathbf{g} = 200$ ,  $\mathbf{g} = 020$ ,  $\mathbf{g} = \bar{2}20$  and  $\mathbf{g} = \bar{2}\bar{2}0$  and the direction of each diffraction vector is illustrated with a white arrow in the image. It is found the labelled dislocations are in contrast for  $\mathbf{g} = 200$ ,  $\mathbf{g} = 020$  and  $\mathbf{g} = \bar{2}\bar{2}0$  but out of contrast for  $\mathbf{g} = \bar{2}20$ . Based on the contrast analysis, the Burgers vector of these dislocations is determined as  $\mathbf{b} = n/2[1\bar{1}0]$ , where  $n$  is an integer. To determine the line direction of dislocations, dislocations were imaged with the beam parallel to [001] and [103] zone axis of the  $\tau$ -grain, as shown in Fig. 3(a) and (f). Two vectors which are perpendicular to the same specified dislocation image in Fig. 3(a) and (f), respectively, could be determined with the corresponding selected area diffraction patterns. Finally, the line direction of specified dislocation will be parallel to the cross product of these two vectors. Based on this method, the line directions of dislocations labelled with A, B, F, G and I are parallel to  $[1\bar{1}0]$ , indicating these dislocations are pure screw dislocations. Dislocations C, E, H and J are mixed dislocations and dislocation D has a large edge component. There is some residual contrast of dislocations shown in Fig. 3(e) resulting from the mixed character of dislocations. The existence of large grains in the as-transformed  $\tau$ -MnAl-C allows the formation of dislocations with long length and a dislocation longer than 2  $\mu\text{m}$  is

found, revealing a long stress field along the direction of dislocation line. Theoretical studies show that the magnetic moment of Mn atoms and the magnetocrystalline anisotropy constant are very sensitive to Mn–Mn distance and  $c/a$  values of  $\tau$ -unit cell, and therefore it is reasonable to expect that the magnetic properties will be locally affected due to changes of the lattice parameters inside the strain field surrounding dislocations [34–36]. Bittner et al. [37] found a higher coercivity is observed in cold worked  $\tau$ -MnAl with higher dislocation density compared to a recovered sample with lower dislocation density and the presence of dislocations will also contribute to a lower initial susceptibility due to the pinning effect of magnetic domain walls. The dislocations observed in Fig. 3 are mostly screw dislocations with long length. Compared to edge dislocations, the presence of screw dislocations will not lead to the change of unit cell volume and the lattice strain introduced are mainly from the strain tensor components  $\epsilon_{xz}$  and  $\epsilon_{yz}$ , which implies  $[11\bar{2}]$  and  $[111]$  directions will be distorted. The elastic strain energy caused by edge dislocation is  $1/(1-\nu)$  times ( $\nu$  is the Poisson ratio) higher than that from screw dislocation based on the isotropic elastic theory [38], implying a weaker interaction between screw dislocation with magnetic domain walls compared to the effect of edge dislocation.

Jog 1 in dislocation A has a pure edge character with the line direction parallel to  $[110]$  and corresponding slip plane is (001). The length of the jog segment is 28.4 nm along  $[110]$ . Due to the large jog length, the gliding of screw dislocations would be pinned at this point and the adjacent screw segments would bow out under the action of an applied stress, which may finally lead to the formation

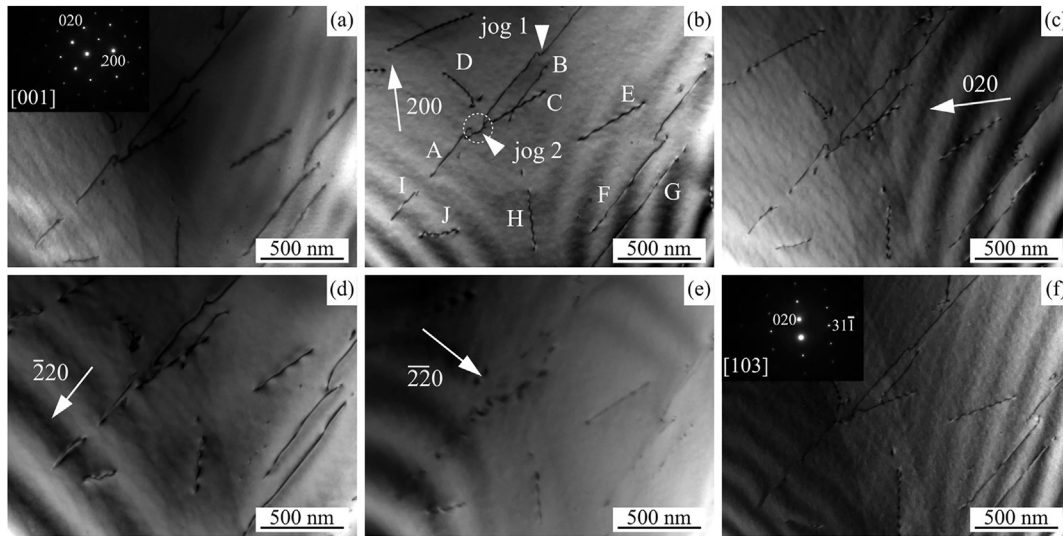


**Fig. 3.** Contrast analysis of dislocations in the as-transformed  $\tau$ -MnAl-C under various diffractions. (a), (f) with the zone axis parallel to  $[001]$  and  $[103]$ . (b)–(e) are bright field images with  $g$  equal to  $g = 200$ ,  $g = 020$ ,  $g = \bar{2}20$ , and  $g = \bar{2}20$ .

of dislocation dipole or act as single-ended dislocation sources [39]. A section of dislocation A which may exhibit this bowing around jog 2 is shown in the dashed white circle in Fig. 3(b).

### 3.2.2. Stacking faults (SF)

SF are frequently observed in the as-transformed  $\tau$ -MnAl-C as shown in Fig. 4. It is reported the formation of SF starts from the growth interface of  $\tau$ -MnAl-C [28]. The different directions of SF in the lower left of the image indicates that more than one fault plane is activated during the phase transformation. Fig. 4(a)–(f) are bright and dark field images of SF under two-beam conditions with the zone axis close to  $[001]$ , and the diffraction vector used is indicated with a white arrow in the corresponding image. Fig. 4(a) and (b) are bright and dark field images using diffraction vector  $g = 200$ . The outer fringe of SF A in the bright field image (Fig. 4(a)) is bright, indicating the phase angle for the fault is  $2\pi/3$ . The top and bottom intersections of the SF with the lamella were determined from the

dark field images shown in Fig. 4(b), as the fringe contrast of the bottom intersection will be changed compared with the bright field image in Fig. 4(a). The diffraction vector in the dark field image (Fig. 4(b)) points towards the bright fringe if the start point of the diffraction vector is placed at the centre of the SF, which suggests it is an intrinsic SF [33]. Fig. 4(c) is a centred dark field (CDF) image of the SF using diffraction vector  $g = \bar{2}00$  to confirm that no outer fringe of the SF is missing. Fig. 4(d)–(f) are also used to determine the fault plane of SF A and it can be observed SF A is out of contrast using the diffraction vector  $g = 220$ . Based on above results and stereographic analysis, the displacement vector of SF A is  $-1/3[1\bar{1}\bar{1}]$ . The appearance of intrinsic SF is equivalent to the insertion of several atomic layers of the  $\epsilon'$ -phase (B19) in the ferromagnetic  $\tau$  phase. Little appears to be known about the exchange coupling at the interface ( $\epsilon'$ -phase and  $\tau$ -phase); however, several studies [40,41] showed that not all SF have domain walls attached to them and that the domain walls rearranged themselves along different sets of SF

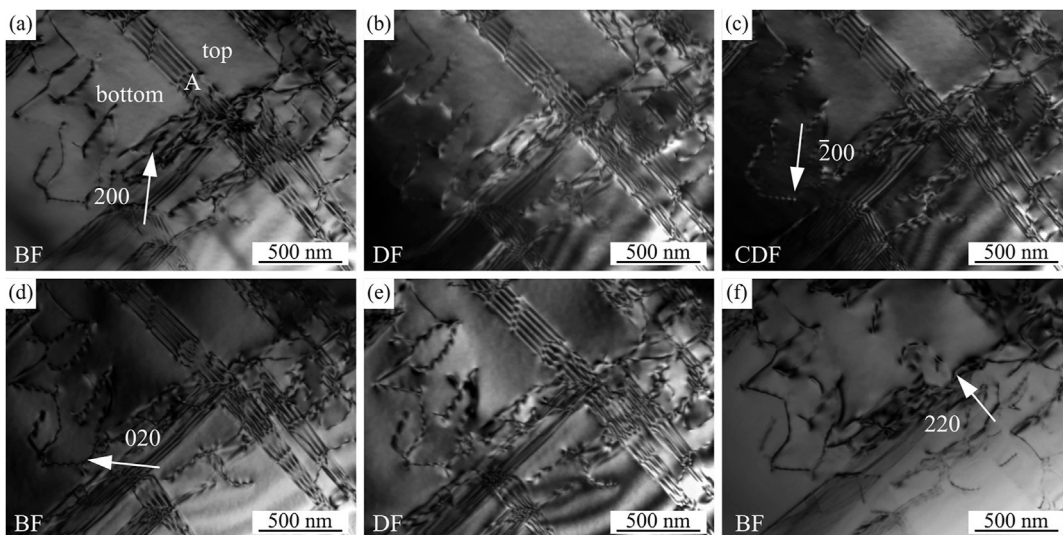


**Fig. 4.** Bright field and dark field images of SF in the as-transformed  $\tau$ -MnAl-C under various diffractions. (a) and (b) bright field and dark field images with  $g$  equal to 200, (c) centred dark field image with  $g$  equals to  $\bar{2}00$ , (d) and (e) bright field and dark field images with  $g$  equal to 020, (f) bright field image with  $g$  equal to 220.

after the application and removal of magnetic field. These results imply that SF may act as pinning sites of domain walls.

### 3.2.3. Micro-twins

Three different twin-like defects in  $\tau$ -MnAl-C have been reported using electron backscattered diffraction (EBSD). These are referred to as true twins, order twins and pseudo twins, and can be described by the misorientation angles of  $180^\circ$ ,  $118^\circ$  and  $62^\circ$  about  $\{111\}$  [25]. Fig. 5 shows a montage of several images of micro-twins in the as-transformed  $\tau$ -MnAl-C grain and corresponding selected area diffraction patterns (SAED). The width of these twins is typically below 20 nm. Fig. 5a is a two-beam bright field image using diffraction vector  $\mathbf{g} = 200$  close to zone axis  $[001]$ . The excitation error  $s_g$  was chosen to be slightly greater than 0 in the bottom half of grain in order to acquire good defect contrast, but  $\mathbf{g}$  varies within the grain due to the existence of random dislocations, which result in changes of local orientation (cf. appearance of micro-twins in the top and bottom halves of the grain in Fig. 5a). Bright and dark fringes can be seen within the micro-twins and similar fringe contrast would result from SF under two beam conditions. In order to distinguish between twins and SF in the current case, the sample was tilted to the  $[011]$  zone axis and selected area diffraction pattern were acquired from these defects, as shown in Fig. 5C-F. Fig. 5A and B show the orientation relationship between grain A and B with  $[0\bar{1}1]_A \parallel [\bar{1}10]_B$  and  $(\bar{1}\bar{1}\bar{1})_A \parallel (\bar{1}\bar{1}\bar{1})_B$ , implying an order twin orientation [42]. From the changes in the orientation of the crystal shown in the diffraction patterns in Fig. 5C-F, it is confirmed that these defects are twins rather than SF. The positions where the diffraction patterns were obtained correspond to the labels shown in Fig. 5a. Based on the diffraction analysis, these micro-twins show a true or pseudo twin relationship. These twins show a total length more than  $7 \mu\text{m}$  and are terminated at the grain boundaries on one side. Similar twin structures were also reported by Yanar et al. [12] in massively transformed  $\tau$ -phase and the formation of the planar defects was attributed to the growth faults produced during atomic attachment at the migrating interfaces. Wiezorek et al. [18] also reported plate-like  $\tau$ -phase could be produced via a hybrid displacive-diffusional mechanism which was associated with the interface of massive transformed  $\tau$ -phase and the parent  $\epsilon$  phase. In both phase transformation mechanisms, strain leads to the motion of partial dislocations, which produce the twins in the microstructure.

### 3.2.4. Antiphase boundaries (APB)

Antiphase boundaries (APB), which have fault vectors of  $1/2 \langle 101 \rangle$ , are believed to act as nucleation sites for reverse domains because of the stronger antiferromagnetic exchange coupling at the interface of APB [3,20,43]. The existence of APB in as-transformed  $\tau$ -MnAl-C has been reported by researchers, but the population reported is not consistent [18,21,28,44,45]. In this study, APB are observed in as-transformed  $\tau$ -MnAl-C alloy as shown in Fig. 6, but the population is much lower compared to other defects like dislocations, twins and SF.

## 3.3. Defect structures of the $\tau$ -phase in hot deformed samples

### 3.3.1. Dislocations in recrystallised grains

Compared to the dislocation density in the non-recrystallised grains, the density of dislocations in recrystallised grains is greatly reduced. Fig. 7 shows two-beam BF and weak beam dark field (WBDF) images of dislocations formed in a recrystallised  $\tau$ -MnAl-C grain. Dislocations marked B-F are visible in the BF images recorded using diffraction vectors  $\mathbf{g} = 200$ ,  $\mathbf{g} = \bar{1}\bar{1}\bar{1}$  and  $\mathbf{g} = 202$ , but invisible with  $\mathbf{g} = \bar{2}\bar{2}0$ . Dislocation A is visible in the BF images recorded using diffraction vectors  $\mathbf{g} = 200$ ,  $\mathbf{g} = \bar{2}\bar{2}0$  and  $\mathbf{g} = 202$ ,

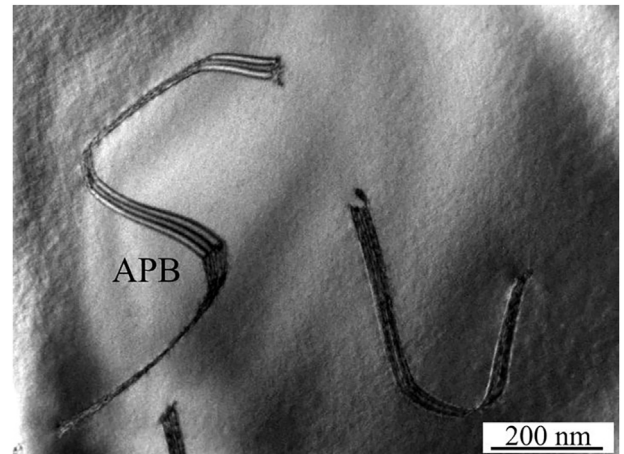


Fig. 6. Antiphase boundary in the as-transformed  $\tau$ -MnAl-C.

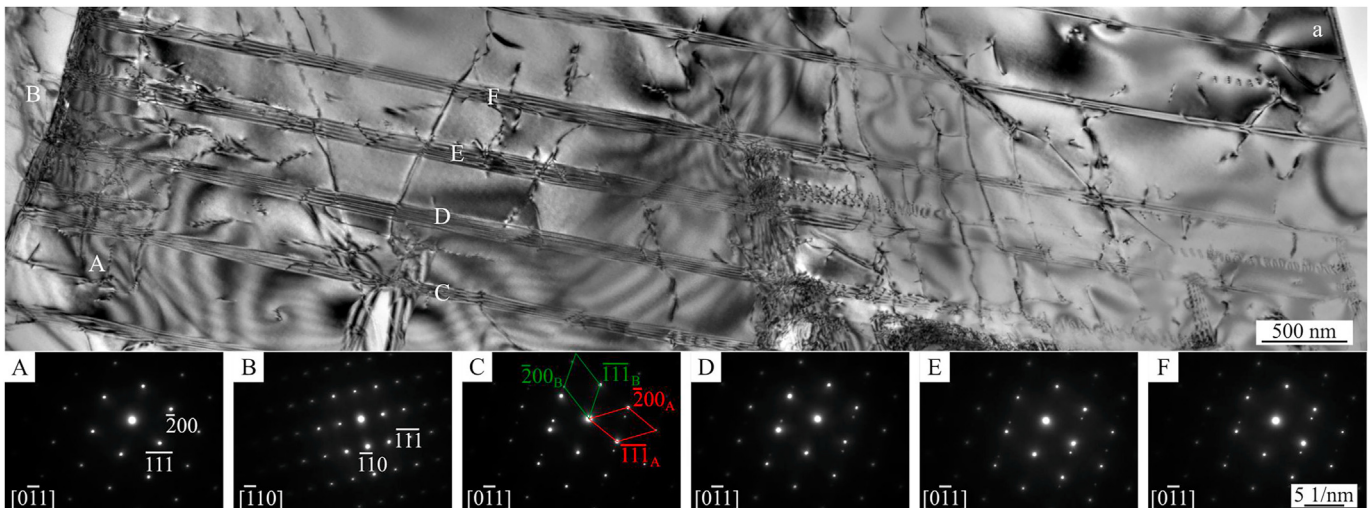
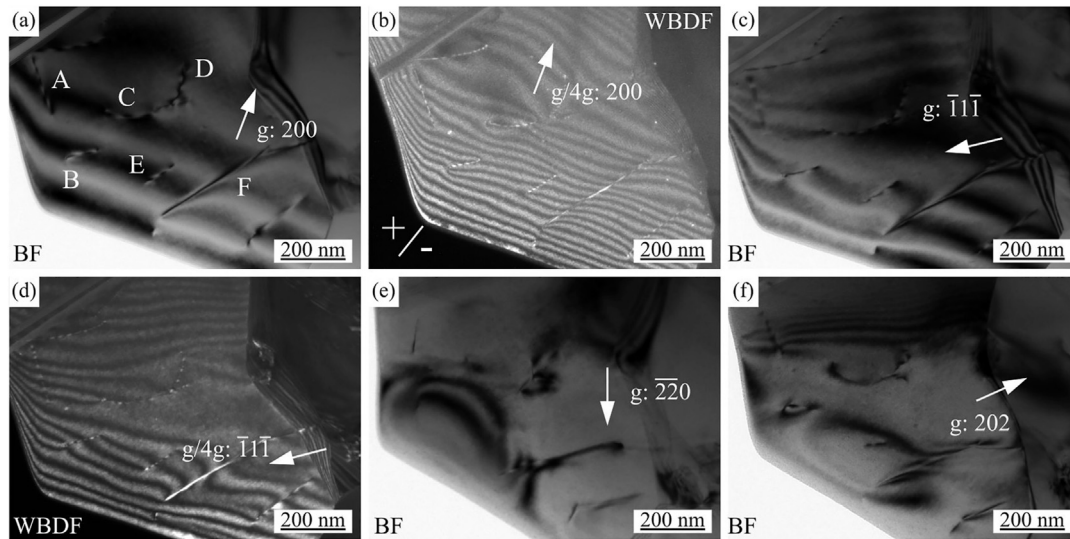


Fig. 5. Twins formed in the as-transformed  $\tau$ -MnAl-C sample and the positions where the diffraction patterns (A to F) were obtained correspond to the labels shown in Fig. 5a.



**Fig. 7.** Contrast analysis of dislocations in the hot deformed  $\tau$ -MnAl-C under various diffractions. a), c), e) and f) bright field images with  $g$  equal to 200,  $\bar{1}\bar{1}\bar{1}$ ,  $\bar{2}\bar{2}\bar{0}$ , and 202 respectively, b) and d) weak beam dark field images ( $g/4g$ ) with  $g$  equal to 200 and  $\bar{1}\bar{1}\bar{1}$  respectively.

but invisible with  $g = \bar{1}\bar{1}\bar{1}$ . As a result, the Burgers vector of dislocations (B-E) belong to  $n/2[1\bar{1}\bar{0}]$ , dislocation A:  $n/2[110]$  and dislocation F:  $n[1\bar{1}\bar{0}]$ , where  $n$  is an integer. To quantify the size and sign of the Burgers vector of these dislocations, weak beam dark field images ( $g/4g$ ) are acquired using 200 and  $\bar{1}\bar{1}\bar{1}$  diffractions shown in Fig. 7(b) and (d). It can be seen in Fig. 7(b) and (d) that the number of fringes terminate at the end of dislocations B to E is  $-1$  and  $+1$  respectively. For the dislocations A and F, the number of fringes terminate at the end of dislocations is  $+1$  and  $-2$  in Figs. 7(b), 0 and  $+2$  in Fig. 7(d). Based on above analysis, the Burgers vector of most of dislocations (A-E) belong to  $1/2[1\bar{1}\bar{0}]$  or  $1/2[110]$  and the Burgers vector of dislocation F is  $[1\bar{1}\bar{0}]$ .

### 3.3.2. Stacking faults in recrystallised grains

After hot deformation, it is not easy to find SF in the sample implying the density of SF was reduced compared to the density in the as-transformed state. Fig. 8 shows BF, DF and centred dark field (CDF) images of SF in the recrystallised grain. The diffraction vectors used for the contrast analysis are indicated and all these diffraction vectors are close to the zone axis  $[001]$ . Two SF are partially overlapped in the centre of the grain with the partial dislocations emitted from the top and bottom boundaries. These two partial dislocations can be seen in all of the images but are most clearly visible in Fig. 8(d), where the SF are out of contrast. From the contrast of the outermost fringes of SF A in the BF and DF images shown in Fig. 8(a) and (b), the top (t) and bottom (b) of the sample can be identified. The diffraction vector used in Fig. 8(a) and (b) is  $\bar{2}00$ , the contrast of the outermost fringe at the bottom of the sample (which is on the right side of SF A labelled with b) will be different. In Fig. 8(b), the diffraction vector will point towards the outermost bright fringe if the start of the vector is placed on the centre of SF A, which indicates SF A is an intrinsic SF. The opposite contrast of the outermost fringe of SF A in the centred dark field (CDF) images using 200 diffraction shown in Fig. 8(c) further proves the outermost fringe contrast of SF A shown in Fig. 8(b). By using  $\bar{2}20$  diffraction vector, it is found that SF A is out of contrast illustrated in Fig. 8(d), which implies  $g_{\bar{2}20} \cdot R = 0$ . In Fig. 8(a), the outermost fringe of SF A is white indicating  $g_{\bar{2}00} \cdot R = +1/3$  or  $-2/3$ . Based on stereographic analysis, the displacement vector of SF

A is  $1/3[1\bar{1}\bar{1}]$  and the stacking sequence of the  $(1\bar{1}\bar{1})$  planes changes to ... ABCABABCABC ... across the fault, which could be considered as insertion of layers of non-magnetic  $\epsilon'$  phase in the  $\tau$  phase region [40,45].

### 3.3.3. Twins in recrystallised grains

Twins are often observed in the  $\tau$ -MnAl-C after hot deformation as shown in Fig. 9. In Fig. 9(a), several twins with sharp interface formed in the recrystallised grain and the width varies from several nm to more than 100 nm. The diffraction pattern in the top right corner of Fig. 9(a) was taken from the dashed circle area and could be indexed with  $[1\bar{1}\bar{0}]$  zone axis showing a true twin relationship. All the twins in this grain are true twins (data are not shown here). In addition to true twins found in the recrystallised grains, an order twin with sharp interface are also observed as shown in Fig. 9(b). As the zone axis of twin and matrix are both parallel to the electron beam, they appear the same diffraction contrast. The diffraction pattern in the top right corner of Fig. 9(b) was taken from the area marked with dashed circle and could be indexed with  $[010]$  zone axis with the misorientation angle about  $86^\circ$ . Considering the symmetry operations of  $\tau$ -MnAl, it is equivalent to  $120^\circ/(111)$ . Due to the limitations of TEM, it is impractical to check all the twin boundaries formed in the samples. In TiAl phase which has the same  $L1_0$  structure as  $\tau$ -MnAl, Inui et al. showed the formation energy ratio of true twin, order twin and pseudo twin is roughly to be 1:2:3 or 1:6:7 to explain why true twins are more common to be observed [42]. Based on the EBSD analysis, Bittner et al. also confirmed true twins are the dominant twin type in  $\tau$ -MnAl-C after hot extrusion [25].

### 3.3.4. Precipitates ( $Mn_3AlC$ )

After hot deformation, precipitates have been observed both within the recrystallised  $\tau$ -grains and at the triple junctions as shown in Fig. 10(a). Due to orientation difference between precipitates A and B, they appear different contrast. The sizes of precipitate A and B are around 240 nm and 150 nm respectively. From the EDXS point analysis, the Mn and Al contents in precipitate A are 70.67 at. % and 29.33 at. %. In precipitate B, the contents of Mn and Al are 62.89 at. % and 37.11 at. %. EDXS elemental mapping in the inset of Fig. 10(a) also showed the whole precipitate B is rich in Mn and deficient in Al with respect to the matrix. Considering the high

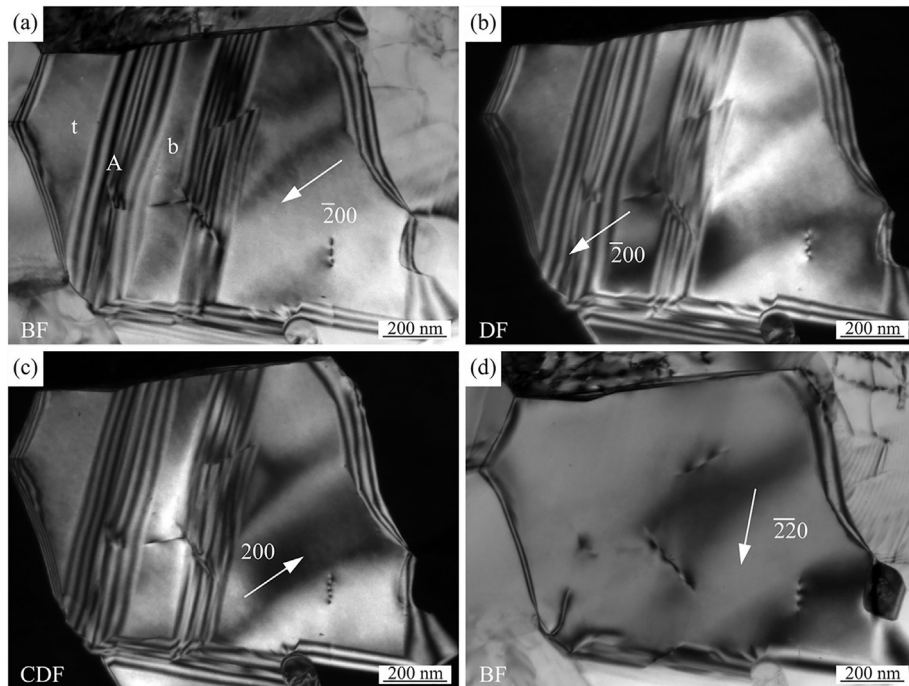


**Fig. 8.** Bright and dark field images of stacking faults in the hot deformed  $\tau$ -MnAl-C under various diffractions. (a) and (b) bright field and dark field images with  $g$  equal to  $\bar{2}00$ , (c) centred dark field image with  $g$  equal to  $200$ , (d) bright field image with  $g$  equal to  $\bar{2}20$ .

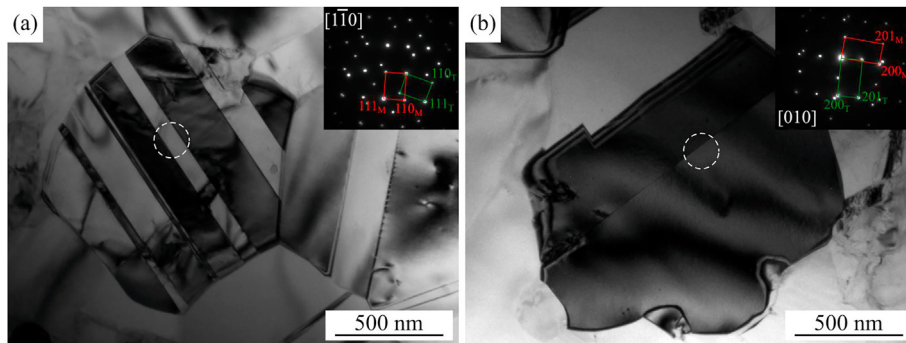


**Fig. 9.** Formation of true twins (a) and order twin (b) in the recrystallised grains of hot deformed  $\tau$ -MnAl-C. The diffraction patterns in the top right corner of Fig. 9 (a) and (b) correspond to the dashed circle in Fig. 9 (a) and (b).

Mn content in precipitates A and B, these two precipitates may be composed of either the carbide  $Mn_3AlC$  ( $Pm\bar{3}m$ , Perovskite) or  $\beta$ -Mn ( $P4_132$ ). Nano-beam diffraction patterns were acquired to determine the crystal structure of the precipitates. A series of nano-beam diffraction patterns of precipitate B is shown in Fig. 10(b)–(e) and they can be indexed as carbide  $Mn_3AlC$  with the zone axis close to  $[\bar{1}\bar{2}\bar{3}]$ ,  $[1\bar{1}\bar{2}]$ ,  $[0\bar{1}\bar{1}]$  and  $[0\bar{1}\bar{3}]$ . The changes in the  $\alpha$  and  $\beta$  tilt angles of the sample holder necessary to rotate the sample from one of the above zone axes to another were transformed into rotation angle/axis pairs. These experimental rotation angles ( $\Delta Exp$ ) matched very well with the calculated angles ( $\Delta Theo$ ) between the above zone axes (Table 1). Although the diffraction patterns in Fig. 10(b)–(e) could also be indexed using the  $\beta$ -Mn structure, different zone axes were found then when indexing with  $Mn_3AlC$ . The experimental rotation angles were not consistent with the calculated angles between the zone axes, when the indexing was carried out with  $\beta$ -Mn. It is therefore concluded that precipitate B is  $Mn_3AlC$  rather than  $\beta$ -Mn. The nano-beam diffraction of precipitate A could be

exclusively indexed by the carbide  $Mn_3AlC$  with the zone axis close to  $[001]$  as shown in the top left of Fig. 10(a); the pattern could not be fitted with  $\beta$ -Mn due to the different lattice parameter. The addition of carbon atoms mainly dissolve interstitially in the  $L1_0$   $\tau$ -MnAl structure and the solubility limit of carbon in the  $\tau$ -MnAl depends on the Mn content [8]. At a Mn content of 53 at.%, the solubility limit of C in the  $\tau$ -phase is approximately 1.4 at.% [46]. Although the carbon content of the materials in this study was nominally 2 at.%, no carbide phases were observed in the as-transformed state, indicating that the actual C-content was approximately equal to the solubility limit. During the dynamic recrystallization process, the solute C-atoms are likely to be rejected to the growth interface. The concentration of C at the boundaries and junctions of the recrystallised grains would therefore increase, facilitating the formation of the  $Mn_3AlC$  phase, whereas the recrystallised grains become somewhat decarburised. This could be confirmed from the lattice parameters refinement on the x-ray diffraction patterns of both states with the  $c/a$  ratio reduced from 0.9289 to 0.9188 (Supplementary Fig. S1). Carbon segregation

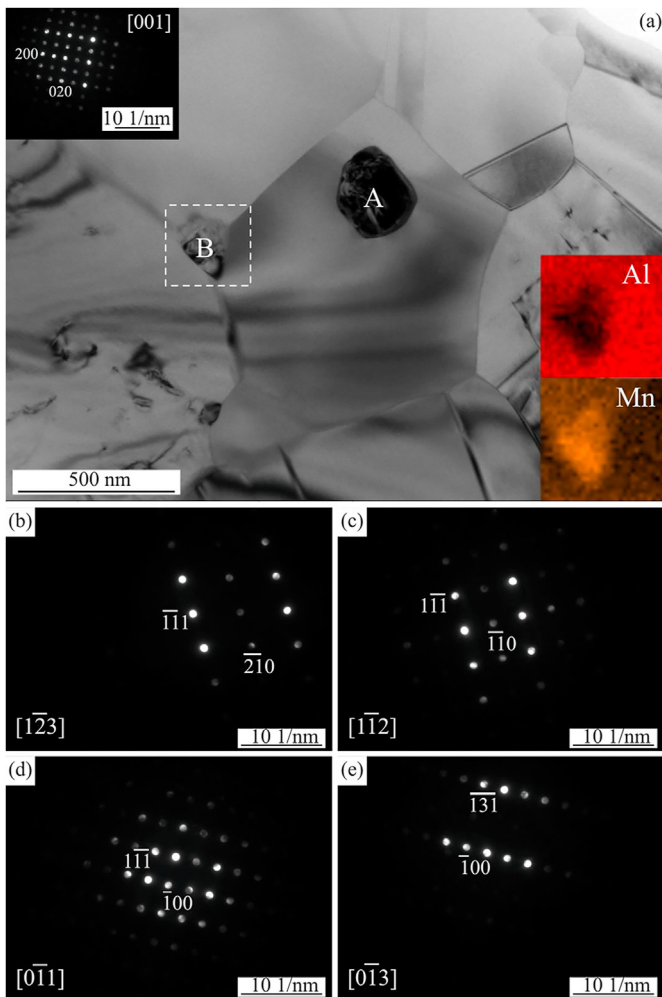


**Fig. 10.** Formation of precipitates ( $Mn_3AlC$ ) in hot deformed  $\tau$ -MnAl-C. The EDXS mapping of precipitate B is positioned in the bottom right of Fig. 10a, the diffraction pattern of precipitate A is shown in the top left of Fig. 10a. Fig. 10b–e shows diffraction patterns of precipitate B.

**Table 1**

Structure determination of precipitates in the hot deformed  $\tau$ -MnAl-C by comparing the angle between two diffraction patterns.

	Stage	Rotation ( $^{\circ}$ )	Tilt Angle ( $^{\circ}$ )	$\Delta(\text{Exp})$ ( $^{\circ}$ )	$\Delta(\text{Theo})$ ( $^{\circ}$ )
B	–5.7	12.3	9.65	10.89	
C	–15	14.9			
B	–5.7	12.3	18.8	19.11	
D	12	5.6			
C	–15	14.9	28.44	30	
D	12	5.6			
D	12	5.6	25.94	26.57	
E	20.5	–19			

or clustering has been observed near the dislocations or grain boundaries in steels using atom probe tomography [47–50]. If this happens in the as-transformed MnAl–C sample, the movement of dislocations may be pinned at these sites. Although some evidence of pinning of dislocations was observed in one region of the as-transformed sample (Supplementary Fig. S2), it was not possible to determine whether the pinning sites were to carbon clusters or nanoscaled  $\epsilon'$  precipitates. In many areas, dislocations did not appear to be pinned. The partial decarburisation of the  $\tau$ -phase is also reflected in the Curie temperature of the hot deformed

material (Fig. 1(b)), which is higher than that of the as-transformed material.  $T_c$  is known to increase with decreasing C-content [51]. Although the decreased Mn content in the  $\tau$  phase also contributes to the decrease of Curie temperature [51], the effect of the change of carbon content on the Curie temperature is likely to be dominant. Furthermore, the  $\tau$ -phase must still contain some C, as its Curie temperature is still lower than that of the binary Mn–Al  $\tau$ -phase, which is expected to be in excess of 600 K [51]. The saturation polarisation of the hot deformed material is lower than that of the as-transformed state (Fig. 1(a)) and this is due to i) the reduction in saturation polarisation corresponding to the reduction in C-content (see [51]), and ii) to the reduction in the volume fraction of the  $\tau$ -phase due to the formation of the carbides.

The formation of fine precipitated carbides has been suggested to benefit coercivity [8,52], however no mechanism has been proposed to explain this. As the  $\tau$ -phase contains less C, its stability against decomposition at elevated temperature is likely to be somewhat reduced. Further heat treatments of hot deformed material may therefore result in faster deterioration of magnetic properties.

### 3.3.5. APB

APB were not observed in the hot deformed  $\tau$ -MnAl-C sample, demonstrating a much lower population compared to other defects after hot deformation. The absence or lower density of APB in hot deformed alloys may be related to the dynamic recrystallization process if each recrystallised grain comes from a single nucleus, there is no mechanism for the formation of APB. The nucleation and pinning fields of magnetic domain walls at defects depend on the strength of magnetic coupling constant at the interface [3,53]. Zijlstra reported for antiferromagnetic coupling at the APB, there is a strong pinning of domain wall and the nucleation field of a domain wall approaches 0 for large negative coupling constant [53]. Lorentz microscopy also showed APB are always decorated with domain walls indicating APB act as nucleation sites for domain walls [21,40,41]. Previous results [21,22,26] and the current work both suggest that the population of APB is very small or non-existent in the hot deformed state. The corresponding reduction in the number of domain wall nucleation sites is likely to contribute to the improvement in the magnetic properties observed in the hot deformed material (Fig. 1).

### 3.3.6. Non-recrystallised grains

A high density of defects is observed in the non-recrystallised grains of  $\tau$ -MnAl-C, due to the accommodation of strain during the hot deformation process. Dislocations, twins and deformation bands are the most commonly observed defects and the microstructure of the non-recrystallised grains is characterized by various different combinations and configurations of these. Fig. 11 shows three different but typical defect structures observed in non-recrystallised  $\tau$ -grains. In Fig. 11(a), a high density of twins is found in two areas A and B, in which the sets of twins are approximately perpendicular to each other. The widths of these twins range from several nm to approx. one hundred nm, and they contain a high density of dislocations. SAED patterns of twins in areas A and B are shown in a1 and a2 of Fig. 11(a), and could be indexed with the  $[1\bar{1}0]$  zone axis showing a true twin orientation. It is interesting to note most of twins in area A show parallel interface on both sides, however the twins in area B have some curvature, and twin edges or tips could be observed, as indicated by the white arrows in Fig. 11(a). The twins in the bottom right portion of area A are segmented along the vertical direction, and it seems like this segment is caused by the hierarchical twinning formed within these twins as similar phenomenon also could be observed for the

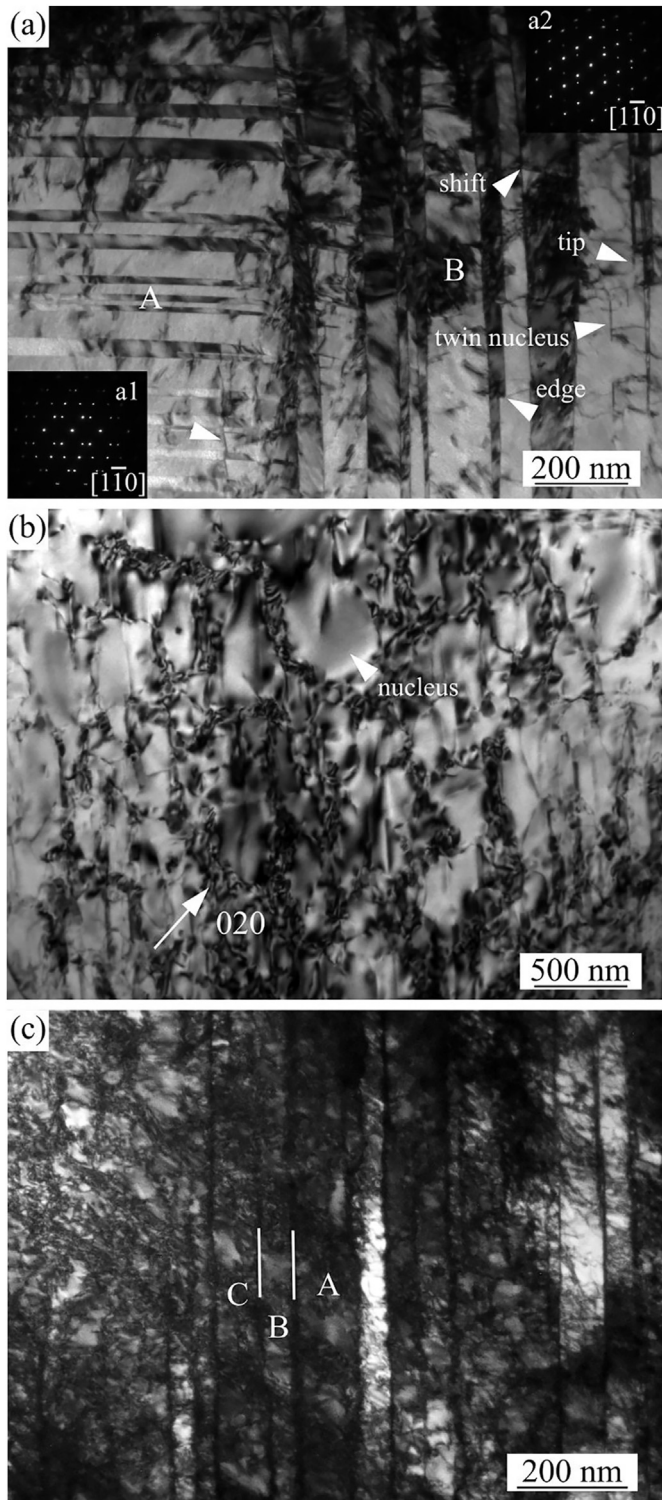


**Fig. 11.** Formation of high density of twins (a), dislocation cells (b) and dislocation walls (c) in the non-recrystallised grains of hot deformed  $\tau$ -MnAl-C.

twins labelled with shift in area B. Two twin nuclei with lenticular shape are formed in area B within the grain [54]. Fig. 11(b) illustrates a bright field image of dislocation cells in the non-recrystallised grains using diffraction vector  $\mathbf{g} = 020$  with the zone axis close to  $[001]$ . These dislocation cells are likely to serve as nuclei of recrystallised grains (indicated by the arrow in the image)

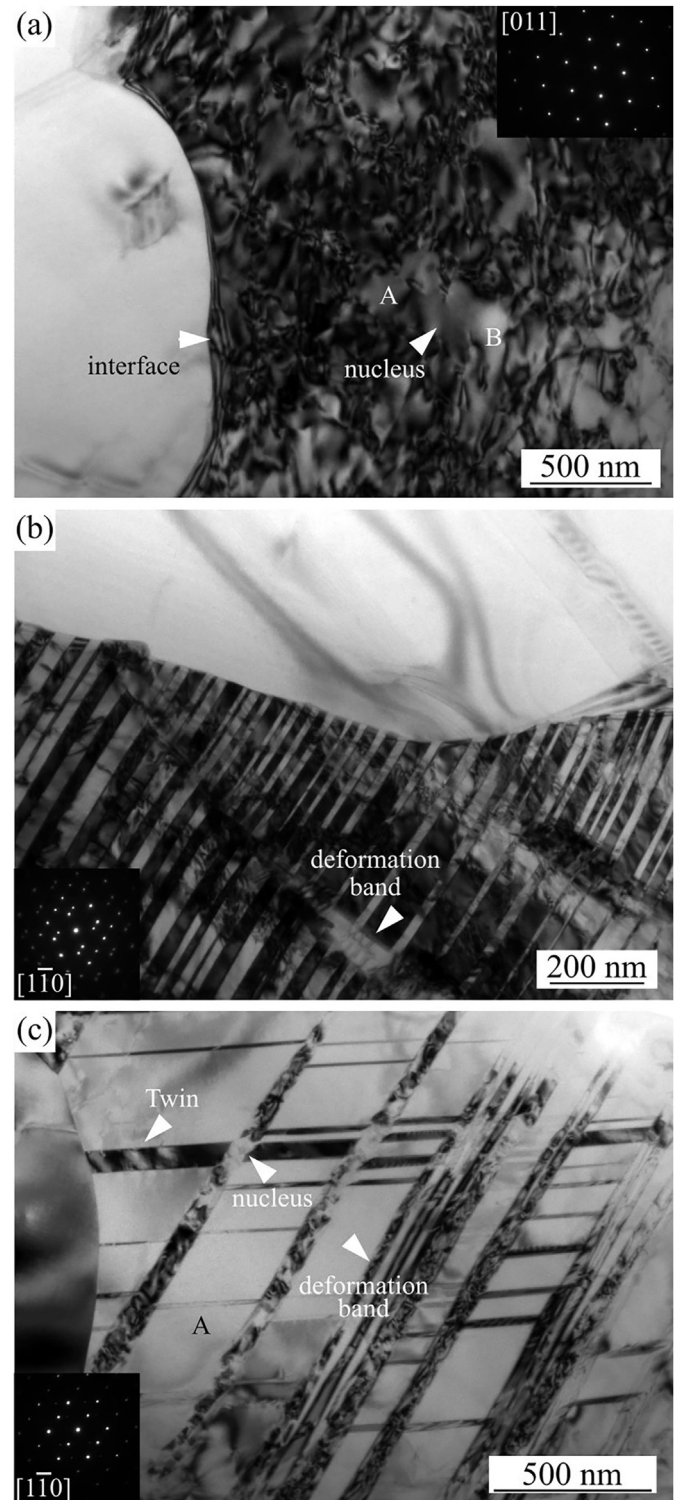


**Fig. 12.** Nuclei and growth of recrystallised grains of hot deformed  $\tau$ -MnAl-C. The growth interface of recrystallised grains into (a) high density of dislocations, (b) highly twinned non-recrystallised regions, and (c) high density of parallel deformation bands.

and the growth of nuclei evolves through consuming dislocation cell walls and merging with its neighbours. A region of a non-recrystallised grain with high dislocation density can be seen in Fig. 11(c). In addition to the complex tangle of dislocations over the entire image, several straight, dark lines can be seen, running from the top of the image to the bottom. Diffraction analysis showed that

**Table 2**  
Defects comparison between as-transformed and the hot deformed  $\tau$ -MnAl-C alloys.

	As-transformed	Hot Deformed	
		Recrystallised grains	Non-recrystallised Grains
Dislocations	Medium density	Low density	High density
Stacking Faults	Many	Few	Not observed
Twins	Many	Medium	High density
APB	Few	Not observed	Not observed
Mn <sub>3</sub> AlC precipitates	Not observed	Many (inter- and intragranular)	Not observed

these are not twin boundaries; the three regions labelled as A, B and C are separated by misorientations with respect to the [110] zone axis of less than 1°. One possible explanation of the vertical dark lines is that they are random arrays of dislocations forming so-called dislocation walls. It is interesting that some nuclei of recrystallised grains could be seen in the grains, which show a different orientation compared to the non-recrystallised grain (small, bright areas in Fig. 11(c)).

Fig. 12 illustrates the growth interface of recrystallised grains during hot deformation. In Fig. 12(a), the growth of recrystallised grain is achieved through the movement of high angle grain boundary towards the non-recrystallised grains with high dislocation density. The non-recrystallised grain could be indexed as  $\tau$ -MnAl-C with the zone axis [011] and in this case, no diffraction spots which would indicate the presence of twins were observed (inset in Fig. 12(a)). Nuclei of recrystallised grains could also be found in the non-recrystallised grain, for example, two nuclei A and B are merging into each other with a small dislocation cell segment left in the middle. In contrast to Fig. 12(a), which showed a non-recrystallised grain without twins, Fig. 12(b) shows a highly twinned (polytwinned) non-recrystallised grain being consumed by a growing recrystallised grain. Based on the orientation analysis from the SAED pattern, the twins in the non-recrystallised grain show a true twin relationship. A deformation band (marked with a white arrow in Fig. 12(b)) can be seen in the non-recrystallised grain, which results in the observed misfit between the upper and lower parts of twins. No nuclei are found in the polytwinned area. Dislocations can be observed within the interior of twins. Fig. 12(c) shows the growth of recrystallised grain (left) into a non-recrystallised grain with parallel deformation bands (running diagonally from bottom left to top right), which themselves contain a high density of dislocations. Several twins formed in the horizontal direction between these bands exhibiting a ladder structure. The inset of Fig. 12(c) is the diffraction pattern of a twin marked with A, showing a true twin relationship. In the middle of the figure, a horizontal twin is cut into several fragments due to the formation of the deformation bands. A small nucleus of recrystallised grain with a different contrast is formed at the intersection of twin and deformation band and consuming its neighbours.

### 3.4. General discussion

Non-recrystallised grains with various defects, especially a high density of true twins, still exist here after hot deformation, which is likely to limit the coercivity. Previous research indicated that non-recrystallised grains exhibit a lower resistance to magnetization reversal [19]. Micromagnetic simulations also confirmed that the presence of various twins will deteriorate coercivity [3]. Suppressing the formation of twins and decreasing the population of non-recrystallised grains would likely result in an improvement in magnetic properties [55]. In this study, it is found that dislocation cells are likely to serve as nuclei of recrystallised grains. Research also found dislocation tangling and cell formation decreases when

SF energy decreases as the distance between partial dislocations increases and cross slip is difficult [56]. Various models proposed to explain the formation of twins suggest the formation of partial dislocations and movement of partial dislocations are directly related to the twin formation [54]. As a result, considering the nucleation role of dislocation cells in  $\tau$ -MnAl-C during dynamic recrystallization, experimenting with various doping elements in order to increase the SF energy can be considered to further increase coercivity of  $\tau$ -MnAl alloy. Finally, based on the defect characterisation using TEM, the difference of various defects qualitatively in the as-transformed and hot deformed state is illustrated in Table 2.

## 4. Conclusions

The significant improvement in magnetic properties observed after die upsetting an as-transformed sample of  $\tau$ -MnAl-C is accompanied by large changes in the microstructure. The higher remanence measured perpendicular to the direction of deformation results from the formation of a planar  $\langle 001 \rangle$  texture. The higher coercivity results mainly from a dramatic reduction of the grain size from 100s of  $\mu\text{m}$  to  $<1 \mu\text{m}$ . The absence of APB in the hot deformed state may also contribute to improving the magnetic properties. The difference in Curie temperature between the two states can be explained by the partial decarburisation of the  $\tau$ -phase which accompanies the formation of Mn<sub>3</sub>AlC inter- and intragranular precipitates in the hot deformed material. Dislocations with Burger's vectors  $1/2[1\bar{1}0]$  or  $1/2[110]$ , intrinsic stacking faults on {111} planes and true twins were observed in the fine, recrystallised grains but the density of these defects was generally lower than in the as-transformed state. The non-recrystallised grains in the hot deformed material exhibited various complex microstructures based on combinations of dislocations, true twins and deformation bands. Highly twinned non-recrystallised grains are likely to have a detrimental effect on the coercivity of the material. For a further improvement in magnetic properties, advanced processing techniques should be explored to further increase the texture formation of  $\langle 001 \rangle$  and the population of larger non-recrystallised grains should be reduced or eliminated.

### Data availability

The data are available from the corresponding author on reasonable request.

### CRediT authorship contribution statement

**P. Zhao:** Methodology, Formal analysis, Writing - original draft, Experimental work and data analysis, Writing Original Draft. **L. Feng:** Writing - review & editing, Hot deformation test and Magnetic properties measurement, Review. **K. Nielsch:** Writing - review & editing, Review, Supervision. **T.G. Woodcock:** Conceptualization, Methodology, Formal analysis, Writing - review & editing, Review & Editing, Supervision, Funding acquisition.

## Declaration of competing interest

The authors declare that they have no known competing financial interests or personal relationships that could have appeared to influence the work reported in this paper.

## Acknowledgements

The authors thank B. Gebel, C. Damm, A. Pöhl, T. Walter, Dr. D. Wolf and Dr. T. Gemming for experimental assistance. This work was funded by the Deutsche Forschungsgemeinschaft (DFG, German Research Foundation) - project no. 326646134.

## Appendix A. Supplementary data

Supplementary data to this article can be found online at <https://doi.org/10.1016/j.jallcom.2020.156998>.

## References

- [1] R. Skomski, J.M.D. Coey, Magnetic anisotropy - how much is enough for a permanent magnet? *Scripta Mater.* 112 (2016) 3–8.
- [2] J.M.D. Coey, New permanent magnets; manganese compounds, *J. Phys. Condens. Matter* 26 (2014), 064211.
- [3] S. Bance, F. Bittner, T.G. Woodcock, L. Schultz, T. Schrefl, Role of twin and anti-phase defects in MnAl permanent magnets, *Acta Mater.* 131 (2017) 48–56.
- [4] A.D. Crisan, F. Vasiliu, R. Nicula, C. Bartha, I. Mercioniu, O. Crisan, Thermodynamic, structural and magnetic studies of phase transformations in MnAl nanocomposite alloys, *Mater. Char.* 140 (2018) 1–8.
- [5] J. Cui, M. Kramer, L. Zhou, F. Liu, A. Gabay, G. Hadjipanayis, B. Balasubramanian, D. Sellmyer, Current progress and future challenges in rare-earth-free permanent magnets, *Acta Mater.* 158 (2018) 118–137.
- [6] R.W. McCallum, L. Lewis, R. Skomski, M.J. Kramer, I.E. Anderson, Practical aspects of modern and future permanent magnets, *Annu. Rev. Mater. Res.* 44 (2014) 451–477.
- [7] K. Patel, J. Zhang, S. Ren, Rare-earth-free high energy product manganese-based magnetic materials, *Nanoscale* 10 (2018) 11701–11718.
- [8] T. Ohtani, N. Kato, S. Kojima, K. Kojima, Y. Sakamoto, I. Konno, M. Tsukahara, T. Kubo, Magnetic properties of Mn-Al-C permanent magnet alloys, *IEEE Trans. Magn.* 13 (1977) 1328–1330.
- [9] J.M.D. Coey, Permanent magnets: Plugging the gap, *Scripta Mater.* 67 (2012) 524–529.
- [10] F. Bittner, L. Schultz, T.G. Woodcock, The role of the interface distribution in the decomposition of metastable  $L1_0$ - $Mn_{54}Al_{46}$ , *J. Alloys Compd.* 727 (2017) 1095–1099.
- [11] Z. Xiang, Baiwen Deng, X. Zhang, X. Wang, E. Cui, L. Yu, Y. Song, W. Lu, Nanocrystalline MnAlV rare-earth-free permanent magnetic alloys with improved magnetization and thermal stability, *Intermetallics* 116 (2020) 106638.
- [12] C. Yanar, J.M.K. Wiezorek, W.A. Soffa, V. Radmilovic, Massive transformation and the formation of the ferromagnetic  $L1_0$  phase in manganese-aluminum-based alloys, *Metall. Mater. Trans.* 33 (2002) 2413–2423.
- [13] D.P. Hoydick, E.J. Palmiere, W.A. Soffa, Microstructural development in MnAl-base permanent magnet materials: new perspectives, *J. Appl. Phys.* 81 (1997) 5624–5626.
- [14] D.P. Hoydick, E.J. Palmiere, W.A. Soffa, On the formation of the metastable  $L1_0$  phase in manganese-aluminum-base permanent magnet materials, *Scripta Mater.* 36 (1997) 151–156.
- [15] A.S. Sologubenko, P. Müllner, H. Heinrich, G. Kosterz, On the plate-like tau-phase formation in MnAl-C alloys, *Z. Metallkd.* 97 (2004) 205–216.
- [16] P. Müllner, B.E. Bürgler, H. Heinrich, A.S. Sologubenko, G. Kosterz, Observation of the shear mode of the  $\epsilon \rightarrow \tau$  phase transformation in a Mn-Al-C single crystal, *Phil. Mag. Lett.* 82 (2002) 71–79.
- [17] J.J. Van Den Broek, H. Donkersloot, G. Van Tendeloo, A.J.V. Landuyt, Phase transformations in pure and carbon-doped  $Al_{45}Mn_{55}$  alloys, *Acta Metall.* 27 (1979) 1497–1504.
- [18] J.M.K. Wiezorek, A.K. Kulovits, C. Yanar, W.A. Soffa, Grain boundary mediated displacive-diffusional formation of  $\tau$ -phase MnAl, *Metall. Mater. Trans.* 42 (2010) 594–604.
- [19] J. Thielsch, F. Bittner, T.G. Woodcock, Magnetization reversal processes in hot-extruded  $\tau$ -MnAl-C, *J. Magn. Magn. Mater.* 426 (2017) 25–31.
- [20] P. Nieves, S. Arapan, T. Schrefl, S. Cuesta-Lopez, Atomistic spin dynamics simulations of the MnAl  $\tau$ -phase and its antiphase boundary, *Phys. Rev. B* 96 (2017) 22441.
- [21] J.V. Landuyt, G.V. Tendeloo, J.J.V.D. Broek, H. Donkersloot, H. Zijlstra, Defect structure and magnetic properties of MnAl permanent magnet materials, *IEEE Trans. Magn.* 14 (1978) 679–681.
- [22] E.L. Houseman, J.P. Jakubovics, Electron microscope study of the domain structure of MnAlC magnets, *J. Magn. Magn. Mater.* 31–34 (1983) 1007–1008.
- [23] M. Gusenbauer, J. Fischbacher, A. Kovacs, H. Oezelt, S. Bance, P. Zhao, T.G. Woodcock, T. Schrefl, Automated meshing of electron backscatter diffraction data and application to finite element micromagnetics, *J. Magn. Magn. Mater.* 486 (2019), 165256.
- [25] F. Bittner, L. Schultz, T.G. Woodcock, Twin-like defects in  $L1_0$  ordered  $\tau$ -MnAl-C studied by EBSD, *Acta Mater.* 101 (2015) 48–54.
- [26] J. Gau, R. Mishra, G. Thomas, Electron microscopy of Mn-Al-C magnets, *IEEE Trans. Magn.* 19 (1983) 2256–2260.
- [27] X.D. Zhang, S. Godfrey, M. Weaver, M. Strangwood, P. Threadgill, M.J. Kaufman, M.H. Loretto, The massive transformation in Ti-Al alloys: mechanistic observations, *Acta Mater.* 44 (1996) 3723–3734.
- [28] C. Yanar, V. Radmilovic, W.A. Soffa, J.M.K. Wiezorek, Evolution of microstructure and defect structure in  $L1_0$ -ordered manganese aluminide permanent magnet alloys, *Intermetallics* 9 (2001) 949–954.
- [29] Y. Sakamoto, S. Kojima, K. Kojima, T. Ohtani, T. Kubo, Crystal orientation and its formation process of an anisotropic Mn-Al-C permanent magnet, *J. Appl. Phys.* 50 (1979) 2355–2357.
- [30] A. Aharoni, Demagnetizing factors for rectangular ferromagnetic prisms, *J. Appl. Phys.* 83 (1998) 3432–3434.
- [31] Y. Ishida, H. Ishida, K. Kohra, H. Ichinose, Determination of the Burgers vector of a dislocation by weak-beam imaging in a HVEM, *Philos. Mag. A* 42 (1980) 453–462.
- [32] N. Miyajima, N. Walte, Burgers vector determination in deformed perovskite and post-perovskite of  $CaIrO_3$  using thickness fringes in weak-beam dark-field images, *Ultramicroscopy* 109 (2009) 683–692.
- [33] D.B. Williams, C.B. Carter, *Transmission Electron Microscopy A Textbook for Materials Science*, Springer Science and Business Media, New York, 2009.
- [34] A. Edström, J. Chico, A. Jakobsson, A. Bergman, J. Ruzs, Electronic structure and magnetic properties of  $L1_0$  binary alloys, *Phys. Rev. B* 90 (2014).
- [35] J.H. Park, Y.K. Hong, S. Bae, J.J. Lee, J. Jalli, G.S. Abo, N. Neveu, S.G. Kim, C.J. Choi, J.G. Lee, Saturation magnetization and crystalline anisotropy calculations for MnAl permanent magnet, *J. Appl. Phys.* 107 (2010), 09A731.
- [36] A. Sakuma, Electronic structure and magnetocrystalline anisotropy energy of MnAl, *J. Phys. Soc. Jpn.* 63 (1994) 1422–1428.
- [37] F. Bittner, J. Freudenberger, L. Schultz, T.G. Woodcock, The impact of dislocations on coercivity in  $L1_0$ -MnAl, *J. Alloys Compd.* 704 (2017) 528–536.
- [38] D. Hull, D.J. Bacon, *Introduction to Dislocations*, fifth ed., Butterworth-Heinemann, Oxford, 2011.
- [39] U. Messerschmidt, *Dislocation Dynamics during Plastic Deformation*, Springer-Verlag Berlin Heidelberg, 2010.
- [40] J.P. Jakubovics, A.J. Lapworth, T.W. Jolly, Electron microscope studies of ferromagnetic ordered structures, *J. Appl. Phys.* 49 (1978) 2002–2006.
- [41] J.P. Jakubovics, T.W. Jolly, The effect of crystal defects on the domain structure of Mn-Al alloys, *Phys. B* 86–88 (1977) 1357–1359.
- [42] H. Inui, M.H. Oh, A. Nakamura, M. Yamaguchi, Ordered domains in TiAl coexisting with  $Ti_3Al$  in the lamellar structure of Ti-rich tial compounds, *Philos. Mag. A* 66 (1992) 539–555.
- [43] S. Arapan, P. Nieves, S. Cuesta-López, M. Gusenbauer, H. Oezelt, T. Schrefl, E.K. Delczeg-Czirjak, H.C. Herper, O. Eriksson, Influence of antiphase boundary of the MnAl  $\tau$ -phase on the energy product, *Phys. Rev. Mater.* 3 (2019).
- [44] A.V. Dobromyslov, A.E. Ermakov, N.T. Taluts, M.A. Uimin, Electron microscopy investigation of phase transformations in Mn-Al-C alloy, *Phys. Status Solidi* 88 (1985) 443–454.
- [45] E.L. Houseman, J.P. Jakubovics, Domain-structure and magnetization processes in MnAl and MnAlC alloys, *J. Magn. Magn. Mater.* 31–4 (1983) 1005–1006.
- [46] T. Kubo, T. Ohtani, S. Kojima, N. Kato, K. Kojima, E.A. Sakamoto Y, *Machinable Anisotropic Permanent Magnets of Mn-Al-C Alloys*, US3976519A, 1976. United States.
- [47] J. Wang, P.D. Hodgson, I. Bikmukhametov, M.K. Miller, I. Timokhina, Effects of hot-deformation on grain boundary precipitation and segregation in Ti-Mo microalloyed steels, *Mater. Des.* 141 (2018) 48–56.
- [48] A. Vieweg, E. Povoden-Karadeniz, G. Ressel, P. Prevedel, T. Wojcik, F. Mendez-Martin, A. Stark, J. Keckes, E. Kozeschnik, Phase evolution and carbon redistribution during continuous tempering of martensite studied with high resolution techniques, *Mater. Des.* 136 (2017) 214–222.
- [49] F.G. Caballero, M.K. Miller, C. Garcia-Mateo, C. Capdevila, S.S. Babu, Redistribution of alloying elements during tempering of a nanocrystalline steel, *Acta Mater.* 56 (2008) 188–199.
- [50] J. Wilde, A. Cerezo, A.G.D.W. Smith, Three-dimensional atomic-scale mapping of a Cottrell atmosphere around a dislocation in iron, *Scripta Mater.* 43 (2000) 39–48.
- [51] L. Pareti, F. Bolzoni, F. Leccabue, A.E. Ermakov, Magnetic anisotropy of MnAl and MnAlC permanent magnet materials, *J. Appl. Phys.* 59 (1986) 3824–3828.
- [53] H. Zijlstra, Coping with Brown's paradox: the pinning and nucleation of magnetic domain walls at antiphase boundaries, *IEEE Trans. Magn.* 15 (1979) 1246–1250.
- [54] Y.T. Zhu, X.Z. Liao, X.L. Wu, Deformation twinning in nanocrystalline materials, *Prog. Mater. Sci.* 57 (2012) 1–62.
- [56] S. Ighong, C. Laird, Mechanisms of slip mode modification in F.C.C. solid solutions, *Acta Metall* 38 (1990) 1581–1594.
- [24] M. Gusenbauer, H. Oezelt, J. Fischbacher, A. Kovacs, P. Zhao, T.G. Woodcock, T. Schrefl, Extracting local nucleation fields in permanent magnets using machine learning, *npj Comput. Mater.* 6 (2020) 89.
- [52] C. Muñoz-Rodríguez, L. Feng, E.M. Palmero, T. Mix, J. Rial, F. Olsson,

B. Skárman, H. Vidarsson, P.-O. Larsson, T.G. Woodcock, A. Bollero, Fabrication of bulk  $\tau$  MnAl-C magnets by hot-pressing from  $\epsilon$ -phase gas-atomized and milled powder, *J. Alloys Compd.* 847 (2020) 156361.

[55] L. Feng, J. Freudenberger, T. Mix, K. Nielsch, T.G. Woodcock, Rare-earth-free MnAl-C-Ni permanent magnets produced by extrusion of powder milled from bulk, *Acta Mater.* 199 (2020) 155–168.